RSC Advances

PAPER

View Article Online
View Journal | View Issue

Cite this: *RSC Adv.*, 2026, **16**, 14509

Rational design and synthesis of Co(II), Ni(II) and Cu(II) complexes bearing 1,2,4-triazole scaffold for biological applications

Azza A. Hassoon, *[a] Hamada S. Abulkhair, [bc] Ranim H. Ashour,[d] Mariam M. Abdelsamea,[d] Haidy O. Abdullah,[d] Mona A. Eldesoky,[d] Ali R. Shaban,[d] Philopater John[d] and Eslam A. Ghaith [ae]

The chemistry of 1,2,4-triazole-incorporating compounds and their metal complexes has attracted widespread attention due to their potential therapeutic activities. Therefore, this paper presents the synthesis, characterization, biological studies, and theoretical molecular docking evaluation of 4-amino-3-hydrazino-5-mercapto-1,2,4-triazole (**AHMT**) and its Co(II), Ni(II), and Cu(II) complexes. The proposed structures were confirmed by elemental and spectroscopic analyses, yielding *trans*-N_2S_2 in an equatorial arrangement within an octahedral geometry. Numerous biological studies have been conducted on **AHMT**, **Co(II)-AHMT**, **Ni(II)-AHMT**, and **Cu(II)-AHMT**. The synthesized scaffolds have been screened for their antibacterial activity against various bacterial and fungal species. Notably, **Ni(II)-AHMT** is more potent than the other hybrids. Indeed, the cytotoxic activity of the synthesized hybrids was assessed against four human cancer cell lines: HePG2, MCF-7, HeP-2, and HeLa. The findings revealed that **Ni(II)-AHMT** has the most toxicity with IC_{50} values of 8.70 ± 0.5 μM and 9.72 ± 0.7 μM against MCF-7 and HeLa cell lines, respectively. The enhanced antimicrobial and anticancer activities of the metal complexes relative to the free **AHMT** ligand are attributed to Tweedy's chelation theory, which explains that reduced metal polarity increases lipophilicity and membrane penetration. Mechanistic studies revealed that **Ni(II)-AHMT** induces cell death primarily *via* apoptosis and causes prominent G0/G1 cell-cycle arrest in MCF-7 cells. DNA-binding assays of the synthesized compounds were performed. Additionally, the activity of superoxide dismutase (SOD) in the compounds has also been evaluated using the NBT assay. The free ligand **AHMT** and its nickel complex **Ni(II)-AHMT** demonstrate notable radical-scavenging capacity, achieving 75.8% and 70.2% inhibition, respectively, compared to the reference antioxidant L-ascorbic acid (78.2%). Molecular docking experiments were conducted to understand the binding interactions of **AHMT** and its metal complexes with DNA, β-lactamase, and human serum albumin. The docking simulations were consistent with the *in vitro* findings and suggested that **Ni(II)-AHMT** is a potential DNA groove binder and a potent antimicrobial candidate that merits further *in vivo* investigations.

Received 4th December 2025
Accepted 11th March 2026

DOI: 10.1039/d5ra09383j

rsc.li/rsc-advances

1. Introduction

Recently, there has been a rise in microbial and multidrug resistance in the clinical area, adversely impacting health by causing various diseases due to the ineffectiveness and cytotoxicity of organic-based medications, prolonged infection durations, and elevated mortality rates. To address these issues, it is essential to develop novel pharmaceuticals with broad-spectrum biological activity to effectively eliminate microorganisms. Coordination chemistry addresses this issue by facilitating the creation of metal-coordinated molecules. In the same context, metal complexes containing triazole ligands exhibit a broad spectrum of biological activity, capable of combating resistant bacteria.[1,2] Metal-triazole complexes are more likely to traverse lipid bilayer cell membranes. On the other hand, humans require trace amounts of metals for optimal physiological function, and new studies indicate that incorporating metals into pharmaceuticals can enhance their biological efficacy through chelation.

[a]*Chemistry Department, Faculty of Science, Mansoura University, Mansoura 35516, Egypt. E-mail: azza_ahmed@mans.edu.eg*
[b]*Pharmaceutical Organic Chemistry Department, Faculty of Pharmacy, Al-Azhar University, Nasr City, 11884, Cairo, Egypt*
[c]*Pharmaceutical Chemistry Department, Faculty of Pharmacy, Horus University-Egypt, International Coastal Road, New Damietta 34518, Egypt*
[d]*Forensic Science Program, Faculty of Science, New Mansoura University, New Mansoura 35712, Egypt*
[e]*Chemistry Department, Faculty of Science, New Mansoura University, New Mansoura 35712, Egypt*

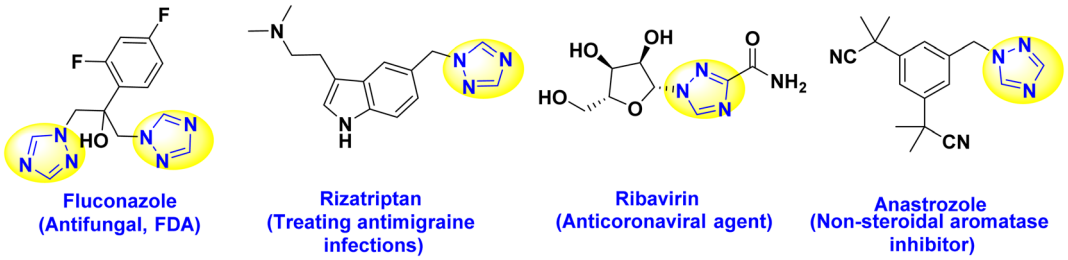

Fig. 1 Marketed drugs based on triazole hybrid.[3–5]

Recently, triazole scaffolds have attracted considerable interest as a prominent field of medicinal and coordination chemistry research due to their high reactivity, biological potential, flexibility, good photostability, and large Stokes shift. In addition, triazole entities are present in various marketed pharmaceutical drugs, including fluconazole, rizatriptan, ribavirin, and anastrozole (Fig. 1) for antifungal activity, treating migraines, an anticoronaviral agent, and a non-steroidal aromatase inhibitor, respectively.[3–5] Also, triazoles can be employed as radiopharmaceutical agents in bioimaging techniques owing to their consequent luminescent properties.[6]

While the structural and electronic features of triazole constitutions enable them to be rigid linking units and be a critical factor in the electronic characters of a peptide bond, without a hydrolytic cleavage effect. In the same context, triazoles exhibit a much stronger dipole moment and dual functionality as hydrogen donors and acceptors, enhancing their extraordinary efficiency in the synthesis of coordination network structures.[6,7]

In particular, 4-amino-3-hydrazino-5-mercapto-1,2,4-triazole (**AHMT**) (Fig. 2), which is commercially available as Purpald, and its derivatives show various pharmacological activities involving promising antifungal,[8] antimicrobial,[9] antitumor agents against hepatocellular carcinoma,[10] pediatric brain tumor,[11] antiviral[12] and tyrosinase inhibitors.[13] On the other hand, **AHMT** has high sensitivity and selectivity properties so that it is utilized as a ratiometric electrochemical sensor for the detection of formalin in residual food samples,[14,15] pesticides,[16] and toxic cations (Cd(II) and Cr(III)[17,18]) in environmental and industrial wastewater. Additionally, many biochemical materials containing picric, uric, and ascorbic acids, as well as lipoic acid, can be easily detected by the **AHMT** sensor.[19]

In contrast to Bagihalli *et al.*,[20] who described Co(II), Ni(II), and Cu(II) complexes with Schiff bases from 3-substituted-4-amino-5-mercapto-1,2,4-triazoles and 8-formyl-7-hydroxy-4-methylcoumarin focusing on antimicrobial effects *via* O,N-donor ligation, and Calu *et al.*,[21] investigated thermal, magnetic, and biological features of Co(II), Ni(II), Cu(II), and Zn(II) complexes with a Schiff base from 3-amino-4*H*-1,2,4-triazole and salicylaldehyde featuring O,N-chelation. The present study pioneers the understudied 4-amino-3-hydrazino-5-mercapto-1,2,4-triazole (**AHMT**) ligand as unique polyfunctional architecture offering versatile N,N,S coordination modes *via* tautomeric thiol–thione (–SH/S), hydrazino (–$NHNH_2$), and amino groups that surpass simple 1,2,4-triazole derivatives, enabling novel distorted octahedral geometries in Co(II), Ni(II), and Cu(II) complexes. Its dual proton donor/acceptor capabilities further foster strong H-bonds (*e.g.*, –NH···S, –SH···O=C stronger than conventional amide bonds) with DNA base pairs, protein side chains, and biological thiols, mimicking sulfur-modified nucleosides/phosphorothioates for enhanced redox biology, enzyme inhibition, and biomolecular interactions beyond the rigid imines of prior works.[22–25] In earlier research, metal complexes of **AHMT** with Pt and Pd;[26] Sn;[27] Ru(II);[28] $[M(CO)_6$ (M = Cr, Mo, W), $Mn(CO)_3Cp]$[28] and oxidovanadium(V)[9] were produced.

While **AHMT** coordination is not entirely unprecedented, preliminary spectral studies date back over 35 years (*e.g.*, Garg *et al.* 1987;[29] Varma *et al.* 1992 [30]), limited to basic IR/UV-vis techniques on select metals (Cu(II),[29,30] Co(II),[29] Ni(II)[29]) without biology. Unlike Garg *et al.* (1987)[29] sulfate-based DMSO–water reflux and Varma *et al.* (1992)[30] alkaline aqueous hot-plate Cu(II) acetate/nitrate synthesis, this introduces chloride salts (including novel $CuCl_2$), neutral methanol reflux (3 : 1 ratio, 8 h at 80 °C), yielding unique octahedral $N_2S_2X_2$ geometries involving thiol-protonated structures with chloride coordination (see Fig. 3) with comprehensive characterization (FTIR, elemental analysis, TGA, conductance, UV-vis, ESR, EI-MS, magnetic moments) absent previously with detailed d–d bands, *g*-values, μ_{eff}, and molecular ions. Most importantly, this is the inaugural report of **AHMT-M(II)** with targeted biological profiles: cytotoxicity, antibacterial effects, DNA binding, superoxide dismutase activity, antioxidants, apoptosis, cell cycle analysis, and docking, transforming foundational chemistry into therapeutic potential.

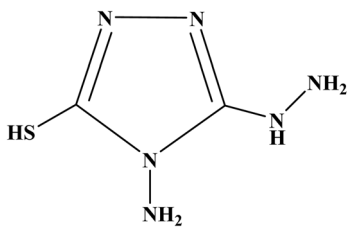

Fig. 2 The chemical structure of AHMT.

2. Experimental

2.1. Materials and instruments

The SI contains detailed information on materials, instruments, and biological studies.

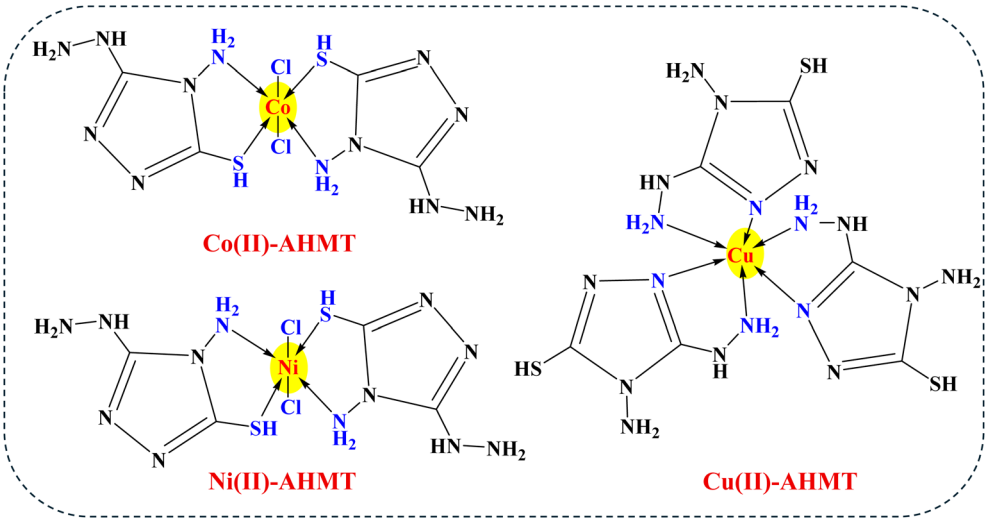

Fig. 3 The chemical structures of the prepared complexes.

2.2. Synthesis of AHMT

The ligand (**AHMT**) (Fig. 2) has been prepared according to the reported methodology[31] as shown in Scheme 1. The structure and purity of the ligand have been confirmed by ^{1}H-NMR in d_6-DMSO and D_2O (Fig. S1 and S2), ^{13}C-NMR (Fig. S3), FT-IR spectrometry (Fig. S4), and CHNS analysis.

AHMT: ^{1}H NMR (DMSO-d_6, 500 MHz): δ (ppm) = 4.09 (br, 2H, NH_2), 5.26 (s, 2H, NH_2), 7.14 (s, 1H, NH), 12.68 (s, 1H, SH); all protons are exchangeable with D_2O; ^{13}C NMR (DMSO-d_6, 125 MHz): δ (ppm) = 164.4 (1C), 154.7 (1C); FT-IR (cm^{-1}): 3263, 3211, 3186, 3075, 3018 (NH_2, NH), 1646 (NH_2), 1591 (C=N), 2920 (S–H), 1456–1281 (C–N + C–C), 1156 (C–S). Color white powder; m.p. 231–233 °C.[31] CHN analysis calcd (%) for $C_2H_6N_6S$ (146.17): C, 16.43; H, 4.14; N, 57.50; S, 21.93; found: C, 16.41; H, 4.19; N, 57.43; S, 22.02. UV/vis λ_{max} (DMSO)/nm: 266.

2.3. Synthesis of metal complexes

Three targeted complexes (Fig. 3) were synthesized by adding a methanolic solution of 4-amino-3-hydrazino-5-mercapto-1,2,4-triazole (**AHMT**) (3 mmol, 0.45 g) to metal chloride ($CoCl_2\cdot6H_2O$, $NiCl_2\cdot6H_2O$, $CuCl_2\cdot2H_2O$, 1 mmol, 0.24 g, 0.24 g, and 0.17 g, respectively) dissolved in a hot methanolic solution. The reactions were refluxed for 8 h at 80 °C.

[Co(**AHMT**)$_2$Cl$_2$]: FT-IR (cm^{-1}): 3292, 3264, 3212, 3181, 3061, 3020 (NH_2, NH), 1648 (NH_2), 1596, 1543 (C=N), 2941 (S–H), 1443–1236 (C–N + C–C), 1158 (C–S). Color brown powder; m.p. > 300 °C. CHN analysis calcd (%) for $C_4H_{12}N_{12}S_2CoCl_2$ (422.18): C, 11.38; H, 2.87; N, 39.81; S, 15.19; found: C, 11.31; H, 3.09; N, 39.62; S, 15.36. μ_{eff} (5.35μ_B) and conductivity: 2.1 Ω^{-1} cm^2 mol^{-1}. UV/vis λ_{max} (DMSO)/nm: 268, 288, 416, 672.

[Ni(**AHMT**)$_2$Cl$_2$]·H$_2$O: FT-IR (cm^{-1}): 3388, 3263, 3210 (NH_2, NH), 1646 (NH_2), 1593 (C=N), 2931 (S–H), 1446–1235 (C–N + C–C), 1196, 1157, 1157 (C–S). Color light green powder; m.p. > 300 °C. CHN analysis calcd (%) for $C_4H_{14}N_{12}OS_2NiCl_2$ (439.95): C, 10.92; H, 3.21; N, 38.20; S, 14.58; found: C, 11.14; H, 3.66; N, 37.32; S, 13.83. μ_{eff} (2.14μ_B) and conductivity: 3.5 Ω^{-1} cm^2 mol^{-1}. UV/vis λ_{max} (DMSO)/nm: 272, 384.

[Cu(**AHMT**)$_3$]Cl$_2$: FT-IR (cm^{-1}): 3264, 3212, 3185, 3076, 3019 cm^{-1} ν(NH_2, NH), 1647 (NH_2), 1594 cm^{-1} (C=N), 2918 cm^{-1} (S–H), 1461–1212 (C–N + C–C), 1157 (C–S). Color grey powder; m.p. 192 °C. CHN analysis calcd (%) for $C_6H_{18}N_{18}S_3$-$CuCl_2$ (572.96): C, 12.58; H, 3.17; N, 44.0; S, 16.79; found: C, 13.59; H, 3.12; N, 44.13; S, 17.67. μ_{eff} (0.99μ_B) and conductivity: 80.3 Ω^{-1} cm^2 mol^{-1}. UV/vis λ_{max} (DMSO)/nm: 268, 296, 556.

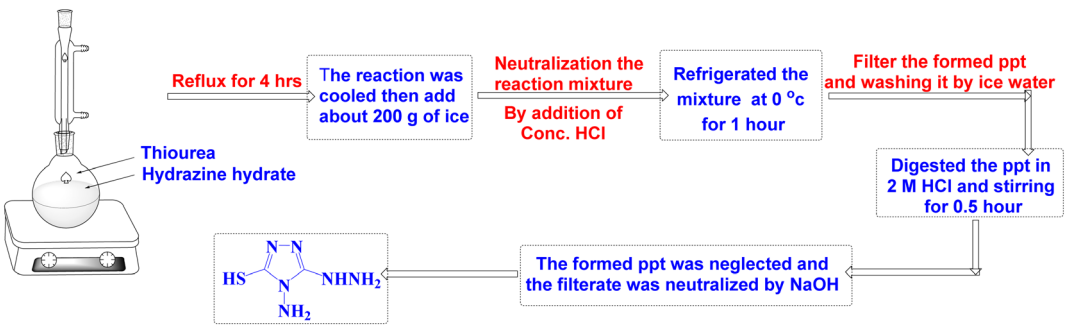

Scheme 1 The outline synthesis of the AHMT ligand.

3. Results and discussion

3.1. General aspects

AHMT was reacted with $CoCl_2$, $NiCl_2$, or $CuCl_2$ at a 3 : 1 ligand/metal ratio, leading to the formation of neutral and cationic complexes with chemical formulae: $[Co(\mathbf{AHMT})_2Cl_2]$, $[Ni(\mathbf{AHMT})_2Cl_2]\cdot H_2O$ and $[Cu(\mathbf{AHMT})_3]Cl_2$ (Fig. 3). The complexes were powdery in appearance and practically insoluble in water as well as in most of the common organic solvents. Conductivity measurements in DMSO indicate the 1 : 2 electrolyte behavior for $[Cu(\mathbf{AHMT})_3]Cl_2$ (80.3 Ω^{-1} cm^2 mol^{-1}),[32] whereas $[Co(\mathbf{AHMT})_2Cl_2]$ and $[Ni(\mathbf{AHMT})_2Cl_2]\cdot H_2O$ (2.1, 3.5 Ω^{-1} cm^2 mol^{-1}, respectively) are non-electrolytes.[32]

3.2. Computational studies

Based on the earlier studies,[33–35] **AHMT** ligand can exist in both thiol and thione forms due to tautomerism (Fig. 4). As shown in Fig. 5, DFT calculations were performed through the Gaussian package confirms that the thiol tautomeric form is a more bioactive coordinator than the other tautomeric form according to the simulated electronic features involving energy gap (ΔE), hardness (η), and softness (S).

$$\Delta E = (E_{HOMO} - E_{LUMO}) \quad (1)$$

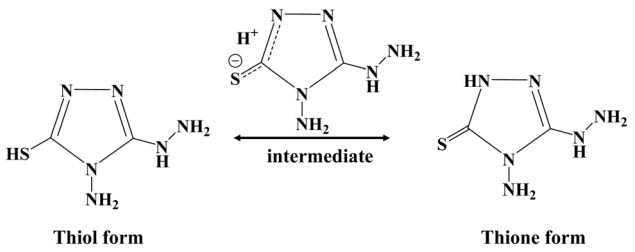

Fig. 4 Thiol and thione forms of AHMT ligand.

$$\eta = 1/2(E_{HOMO} - E_{LUMO}) \quad (2)$$

$$S = 1/\eta \quad (3)$$

As the thiol conformer of **AHMT** ($E_{gap} = -5.686$ eV) displays greater biological and chelation potentiality through thiol and amino functions, compared to the thione conformer ($E_{gap} = -5.465$ eV). On the other hand, the softness as a bioactivity concept assures the relative convergence in the energies, value of both geometrical tautomers of the thiol form with a value ($S = -0.351$) in front of $S = -0.366$ for thione.

3.3. Characterization of the isolated complexes

3.3.1. Vibrational spectra. The important infrared frequencies exhibited by **AHMT** and the isolated complexes are listed in the Experimental section. The ligand molecule contains a tautomeric thioamide moiety: HN–C=S or N=C–SH and hence gives rise to four characteristic bands in the IR spectrum (Fig. S4). These bands are observed around 1456, 1329, 1156, and 650 cm^{-1}. Because of the redistribution of the electron cloud, as a result of complex formation, there is a systematic shift in these bands in the IR spectra of the complexes as compared to those of the ligand (Fig. S1). These shifts are consistent with the coordinating ability of the sulfur atom to metal.[35]

AHMT's IR spectra (Fig. S4) showed characteristic absorption bands at 3263, 3211, 3186, 3075, and 3018 cm^{-1} assigned for NH_2, NH–NH_2 groups,[36,37] 1591, 1281 cm^{-1} corresponded to C=N, C–N groups[36–38] and 2920 cm^{-1} specified for S–H group.[9] Whereby, in the IR spectra of the metal complexes, it was observed that the NH_2 group bands were shifted, indicating binding of the NH_2 group with the metal ion. The characteristic bands for ν(S–H) and ν(C–S) were clearly shifted in the spectra of the **Co(II)-AHMT** and **Ni(II)-AHMT** complexes (Fig. S4), indicating that the thiolic –SH group was still protonated and was

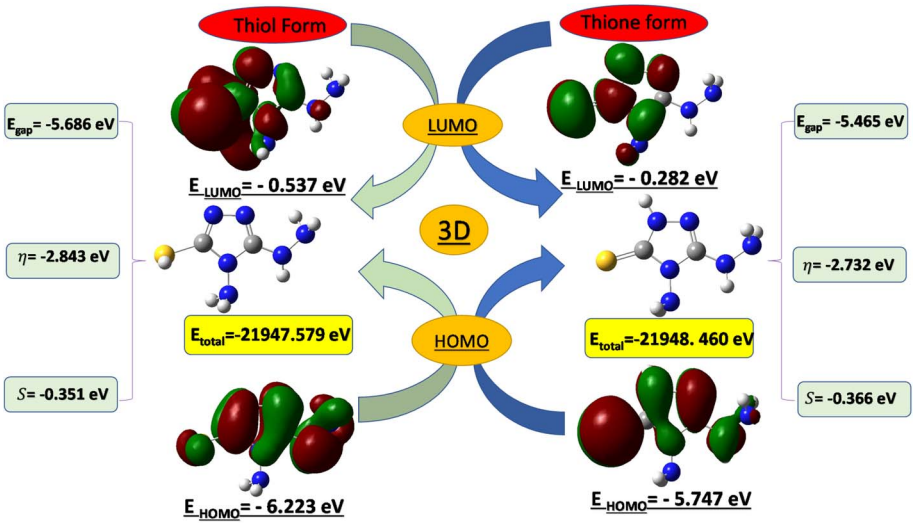

Fig. 5 FMO levels for two tautomeric forms of AHMT and their chemical parameters.

involved in coordination with metal ions.[39,40] Consequently, the coordination environment around the Co and Ni atoms involves NH_2 and SH groups. While ν(C=N) and ν(C–N) bands shifted downward in the **$CuCl_2$-AHMT** complex, indicating that the nitrogenous atom is involved in the coordination to the copper atom. Therefore, the coordination sphere consists of NH_2 and C=N groups around the copper atom. Whereas, a broad medium band is allocated in the range 3200–3500 cm^{-1}, attributable to the ν(O–H) vibration of solvent molecules.[41] The spectra (Fig. S4) showed bands in the 416–544 and 542–668 cm^{-1} regions, which are assigned to ν(M–N) and ν(M–S), respectively.[42,43]

3.3.2. Electronic spectra. The UV spectrum of **AHMT** ligand (Fig. S5) exhibits an absorption peak at 266 nm. This peak arises from the conjugated aromatic triazole ring system. The electronic spectrum of [Co(**AHMT**)$_2$Cl$_2$] (Fig. 6) shows two broad bands in the visible region at 672 nm (14 837 cm^{-1}) and 416 nm (24 038 cm^{-1}) assigned to $^4T_{1g} \rightarrow {}^4A_{2g}$ (ν_2) and $^4T_{1g} \rightarrow {}^4T_{1g}$(P) ($\nu_3$) characteristic for an octahedral geometry. Moreover, the value of the room temperature magnetic moment ($\mu_{eff} = 5.35\mu_B$) is taken as evidence for the existence of one high-spin cobalt atom supporting an octahedral geometry.

The electronic absorption spectrum of [Ni(**AHMT**)$_2$Cl$_2$]·H_2O complex (Fig. S5) shows a sole weak shoulder absorption band at 384 nm, which is attributed to the $^3A_{2g}$(F) $\rightarrow$ $^3T_{1g}$(P) (ν_3) transition, in favor of octahedral geometry. Also, the magnetic moment value of Ni(II) complex assured the presence of two unpaired electrons (d^8) in the octahedral geometry ($2.14\mu_B$). However, the observed magnetic moment of $2.14\mu_B$ is lower than the spin-only value ($\sim 2.83\mu_B$) expected for a high-spin Ni(II) (d^8) complex. It can be concluded that the low μ_{eff} ($2.14\mu_B$) indicates that [Ni(**AHMT**)$_2$Cl$_2$]·H_2O adopts a low-spin configuration in a distorted octahedral geometry, with strong ligand field effects and spin–orbit coupling reducing the number of unpaired electrons. These findings align with studies showing similar magnetic behavior in Ni(II) complexes with strong-field ligands.[44–46]

The electronic absorption spectrum for [Cu(**AHMT**)$_3$]Cl$_2$ complex (Fig. 6) shows a broad band at 556 nm, which corresponds to a d–d transition typical for Cu(II) complexes in a distorted octahedral environment. The magnetic moment (μ_{eff}) of $0.999\mu_B$ is significantly lower than the spin-only value ($\sim 1.73\mu_B$) expected for an isolated Cu(II) ion with one unpaired electron. This reduced magnetic moment indicates strong antiferromagnetic coupling between Cu(II) centers in the complex, likely mediated by bridging ligands or close metal–metal interactions.[44,45]

3.3.3. Thermal gravimetric analysis. The thermogravimetric analysis (TGA) data reveal a three-stage decomposition process for the **Co(II)-AHMT** complex (Fig. S6). In the initial stage (28–60 °C), a 57.30% mass loss aligns closely with the theoretical value of 57.59%, attributed to the release of volatile fragments including Cl_2, 4CN and $2H_2S$. This suggests efficient dehydration and elimination of small molecules at low temperatures. The second stage (60–502 °C) shows a 27.71% loss (theoretical: 28.45%), likely from the release of volatile fragments including $4N_2 + 4H_2$. Finally, the residue (502–800 °C) constitutes 13.96% (theoretical: 14.99%) as metallic cobalt (Co), confirming its thermal stability and role as an end product. The thermogravimetric analysis (TGA) of **Ni(II)-AHMT** complex (Fig. 7) demonstrates a multi-stage decomposition process. In the first stage (28–201 °C), a 12.88% mass loss (theoretical: 12.38%) corresponds to the release of H_2O and HCl, likely from dehydration and elimination of coordinated ligands. The second stage (201–285 °C) shows a 21.89% loss (theoretical: 22.40%), attributed to HCl, N_2, and H_2S, indicating decomposition of nitrogen- and sulfur-containing ligand fragments. At higher temperatures (285–434 °C), 24.54% mass loss (theoretical: 24.57%) arises from 4CN and $2H_2$, reflecting cleavage of cyanide groups and hydrogen evolution. The fourth stage (434–541 °C) involves 17.59% loss (theoretical: 17.98%) due to H_5N_3S, suggesting further breakdown of nitrogen–sulfur hybrid moieties. The final residue (23.10%, theoretical: 22.89%) comprises NiN_3, confirming the formation of a thermally stable nickel-azide compound.

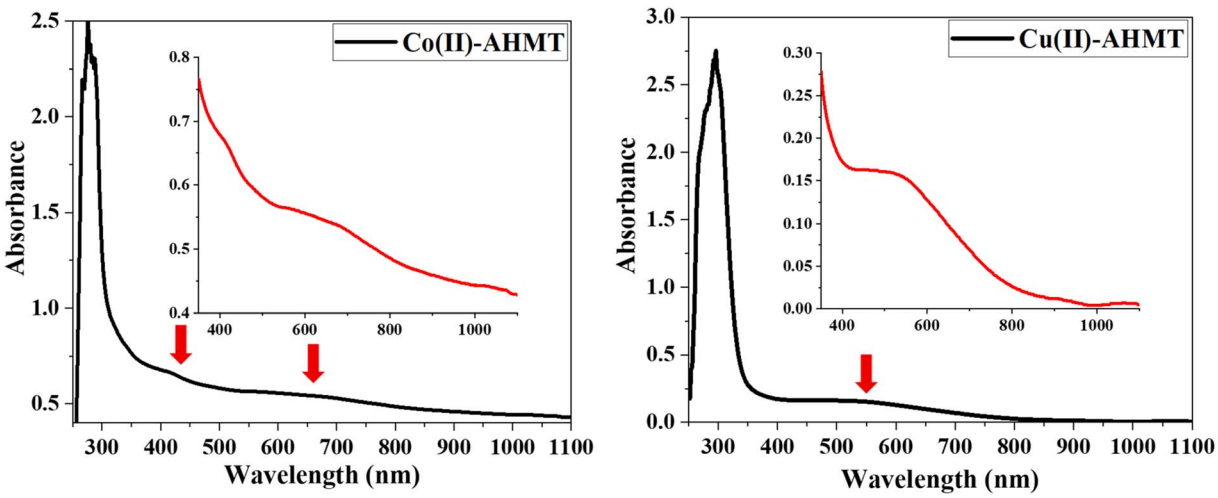

Fig. 6 Electronic spectra of complexes Co(II)-AHMT and Cu(II)-AHMT.

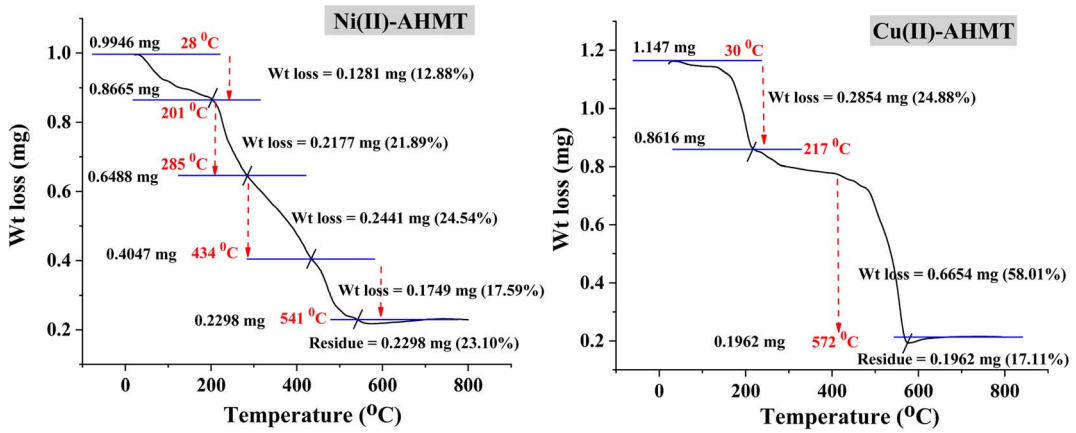

Fig. 7 The TGA curve of Ni(II)-AHMT and Cu(II)-AHMT complexes.

Finally, the thermogravimetric analysis (TGA) of **Cu(II)-AHMT** complex (Fig. 7) reveals a two-stage decomposition process followed by residue formation. The initial stage (30–217 °C) exhibits a 24.88% mass loss (theoretical: 24.95%), attributed to the release of Cl_2, $2N_2$, and NH_2, suggesting the elimination of chlorine-containing ligands and nitrogen-rich fragments. The second stage (217–572 °C) shows a substantial 58.01% loss (theoretical: 58.36%), corresponding to the evolution of $2H_2S$, 6HCN, $3N_2$, NH_4^+, and H_2, indicating the breakdown of sulfur- and nitrogen-based ligands, including hydrogen cyanide and ammonium-related species. The final residue (572–800 °C) constitutes 17.11% (theoretical: 16.68%) as CuS, confirming the formation of a thermally stable copper sulfide compound.

3.3.4. Electron spin resonance. The **Cu(II)-AHMT** complex exhibits an anisotropic ESR spectrum (Fig. 8) with distinct $g_{\parallel}$ (2.10694) and $g_{\perp}$ (2.16285) values, indicative of an axially distorted environment around the Cu(II) ion. This pattern is characteristic of a $d_{x^2-y^2}$ ground state, typically observed for copper(II) ions in distorted octahedral or elongated square planar geometries, and confirms the presence of a tetragonal distortion due to the Jahn–Teller effect. Complementary evidence from ESR parameters, optical absorption features, and magnetic moment measurements persuasively supports the conclusion that the $[Cu(\mathbf{AHMT})_3]Cl_2$ complex adopts a distorted octahedral geometry around the copper(II) ion. This structure is stabilized by the Jahn–Teller effect, which elongates along the *z*-axis and gives rise to the observed spectral and magnetic behaviors.

3.3.5. EI-mass spectrometry. The mass spectra for **Co(II)-AHMT** and **Ni(II)-AHMT** complexes, shown in Fig. S7 and S8, display molecular ion peaks $[M]^+$ at *m*/*z* values of 422.59 and 439.06 with relative abundances of 23.53% and 23.83%, respectively. While the EI-mass spectrum of **Cu(II)-AHMT** exhibits a molecular ion peak [*m*/*z*] at 524.68 with relative abundance 42.57%, which corresponds to the fragment pattern $[M–NH_2–SH]^+$ shown in Fig. S9. These observed peaks closely match the calculated molecular weights, thereby confirming the proposed chemical structures of the complexes.

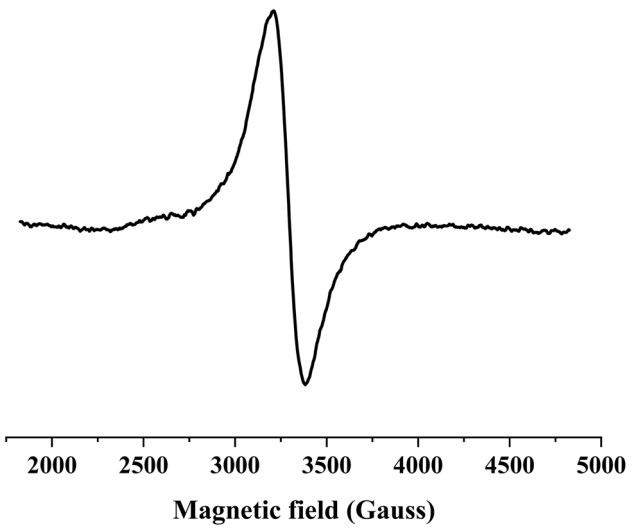

Fig. 8 X-band ESR spectrum of Cu(II)-AHMT.

3.4. Evaluation of biological activity

3.4.1. Antibacterial activity. The **AHMT** ligand and its metal complexes exhibit varying antibacterial and antifungal activity, depending on the coordinated metal ion (Fig. 9, S10 and Table S1). The **AHMT** exhibits moderate antifungal efficacy against *C. albicans* (16 mm inhibition zone, 59.2% activity index compared to clotrimazole), surpassing its antibacterial effects against *E. coli* (9 mm, 34.6%) and *S. aureus* (11 mm, 45.8%). The **Ni(II)-AHMT** combination exhibits the most potent antibacterial activity among the metal complexes, especially against *S. aureus* (14 mm, 58.3% activity index), outperforming the **Cu(II)-AHMT** complex (9 mm, 37.5%) and the **Co(II)-AHMT** complex (5 mm, 20.8%). This indicates that **Ni(II)-AHMT** coordination enhances antibacterial efficacy compared with the unbound ligand. Nonetheless, the ligand alone shows enhanced antifungal efficacy relative to its metal complexes, as evidenced by a larger inhibition zone against *C. albicans* (16 mm *vs.* 8–13 mm for the metal complexes). The diminished activity of the **Co(II)-AHMT** complex against all examined pathogens (3–8 mm inhibitory

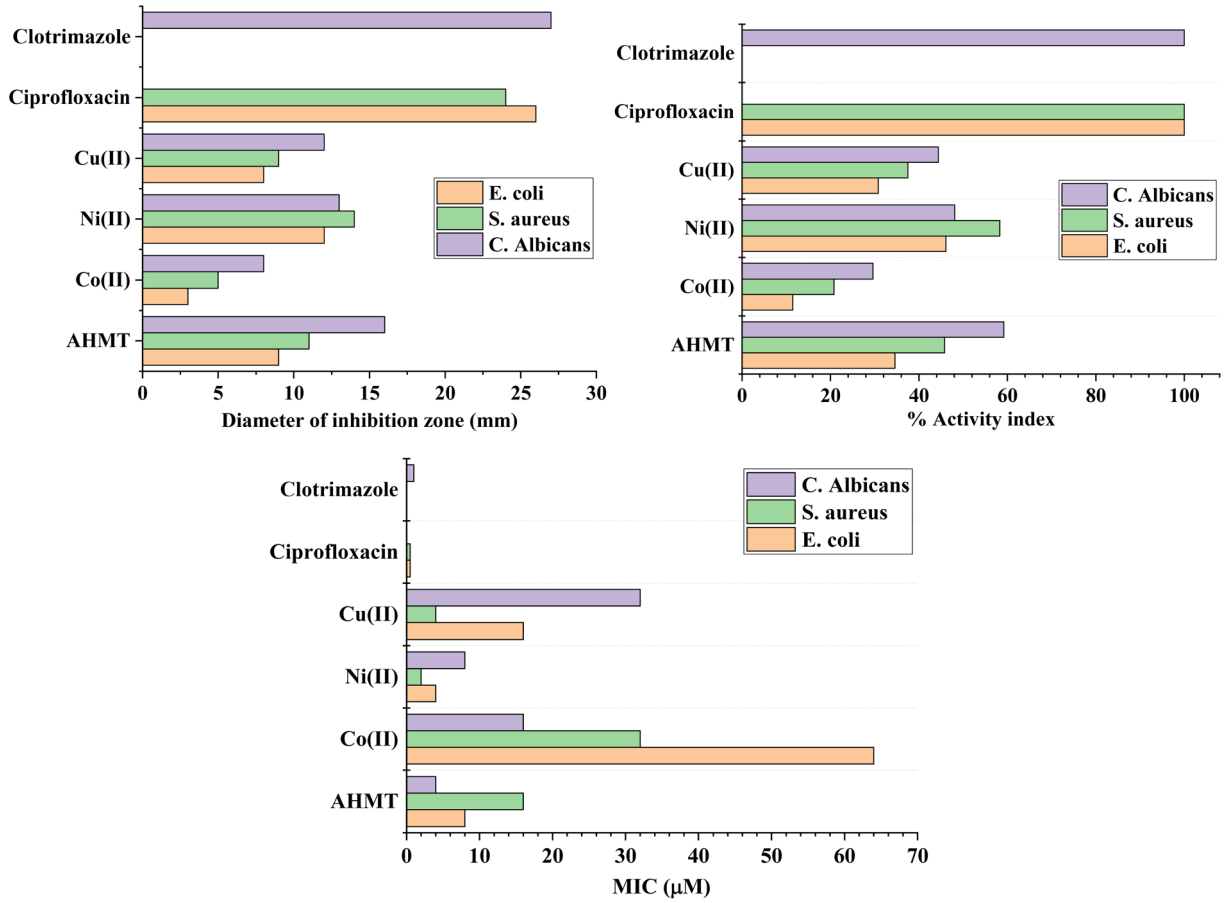

Fig. 9 Antimicrobial activity of AHMT and its metal complexes.

zones) underscores the pivotal importance of metal ion selection in influencing efficacy. These results align with research indicating that 1,2,4-triazole-metal complexes often exhibit superior antibacterial activity compared to their ligands, but the degree of enhancement depends on the metal's electronic and steric properties.[1,47]

The antimicrobial screening revealed a clear correlation between inhibition zone diameters (Fig. 9 and Table S1) and Minimum Inhibitory Concentration (MIC) (Fig. 9 and Table S2).[48,49] The free ligand **AHMT** exhibited moderate antibacterial activity against *E. coli* (MIC = 8 μg mL^{-1}) and *S. aureus* (MIC = 16 μg mL^{-1}), while demonstrating notable antifungal potency against *C. albicans* (MIC = 4 μg mL^{-1}). Upon coordination with metal centers, the biological activity shifted significantly, illustrating the critical role of the metal ion in modulating the antimicrobial profile. The **Ni(II)-AHMT** complex emerged as the most effective agent in this series, demonstrating superior activity against both Gram-negative and Gram-positive bacteria and fungi. Notably, it achieved an MIC of 2 μg mL^{-1} against *S. aureus*, representing an eight-fold increase in potency compared to the free **AHMT** ligand (16 μg mL^{-1}). It also showed strong inhibition against *E. coli* (4 μg mL^{-1}) and *C. albicans* (8 μg mL^{-1}). This broad-spectrum efficacy suggests that the nickel(II) center facilitates optimal membrane permeability and interaction with multiple microbial molecular targets. The **Cu(II)-AHMT** complex showed selective potency against *S. aureus* (4 μg mL^{-1}), though it was less effective against *E. coli* and *C. albicans* compared to the free ligand. Conversely, coordination with Co(II) resulted in a significant reduction in bioactivity (MICs 16–64 μg mL^{-1}), suggesting that the cobalt(II) center may hinder the ligand's biological availability or pharmacophore orientation. The enhanced antimicrobial activity of the metal complexes compared to the free **AHMT** ligand is primarily governed by Tweedy's chelation theory.[50] The partial sharing of the metal ion's positive charge with the ligand's donor groups (N and S atoms) results in a decrease in the polarity of the metal ion and a significant increase in the lipophilicity of the complex. This promotes easier penetration through the lipoid layers of the microbial cell membranes. Furthermore, coordination might enhance the compounds' ability to block the metal-binding sites of microbial enzymes or to interfere with the respiratory chain, ultimately leading to superior inhibitory effects, as evidenced by the lower MIC values.

3.4.2. *In vitro* anticancer activity. The **AHMT** ligand and its metal complexes demonstrate varying cytotoxicity profiles across the tested cancer cell lines (Fig. 10, 11 and Table S3), with metal coordination playing a significant role in determining potency. The **AHMT** exhibits moderate cytotoxicity, especially towards HePG-2 (IC_{50} = 18.01 ± 1.4 μM) and HeLa (21.46 ± 1.5 μM), surpassing the efficacy of its **Cu(II)-AHMT** complex (40.62–

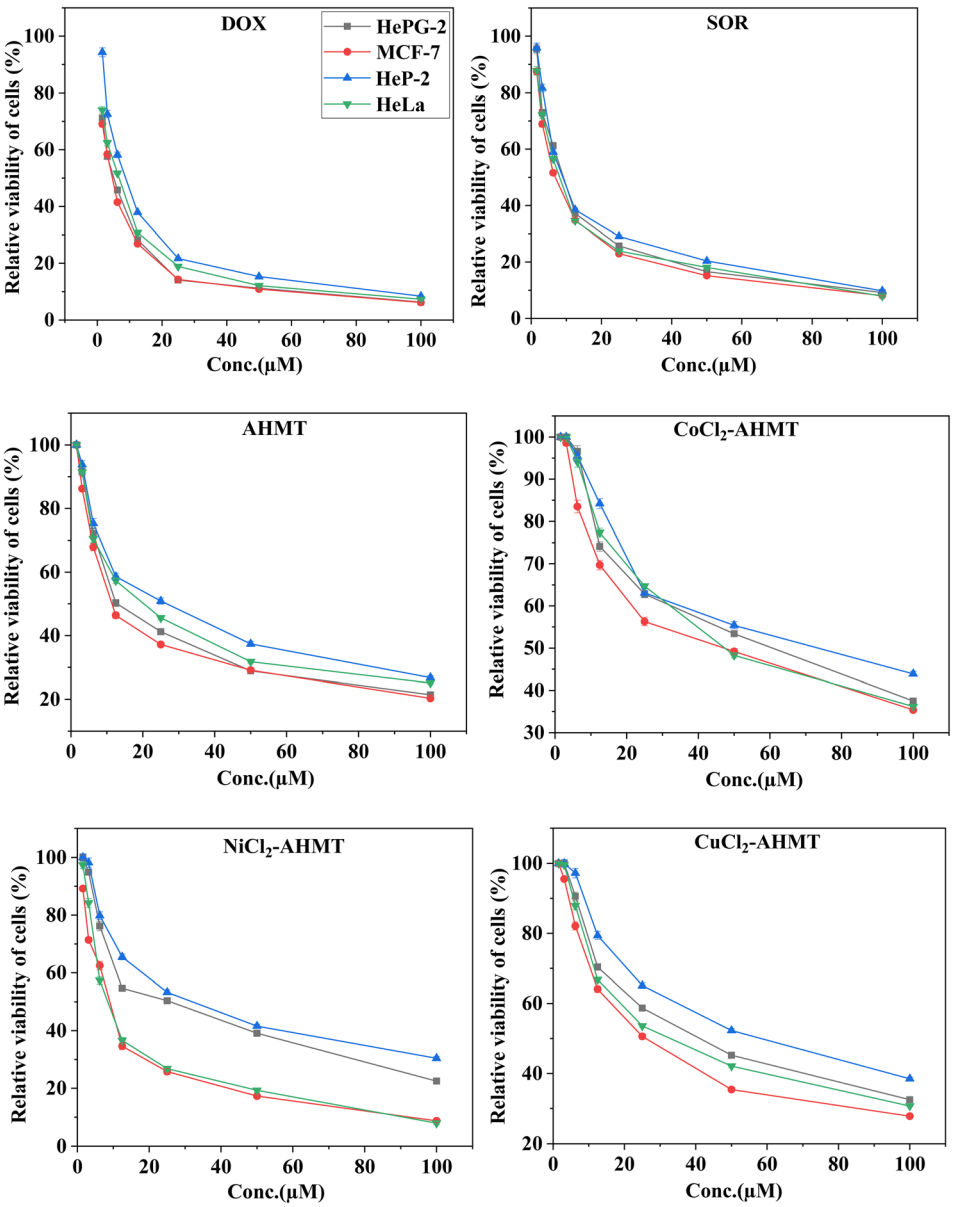

Fig. 10 The plot of series dilutions *versus* cell viability% in cell lines. Each data point represents the mean ± SD ($n = 3$), with statistical significance indicated by (*$p < 0.05$).

55.58 μM) and **Co(II)-AHMT** complex (42.84–64.48 μM). The **Ni(II)-AHMT** complex exhibits significantly increased activity, particularly against MCF-7 (8.70 ± 0.5 μM) and HeLa (9.72 ± 0.7 μM), exceeding the efficacy of both the unbound ligand and the reference drug sorafenib (SOR) in these cell lines. This highlights the role of nickel in enhancing efficacy, potentially attributed to improved DNA interaction or redox activity.[51–53] Notably, the compounds' potential toxicity was assessed using the MTT assay on MCF-10A normal cells. The findings demonstrated low cytotoxicity towards normal cells at concentrations effective against cancer cells, as presented in Fig. 11 and Table S3. Based on Tweedy's chelation theory,[50] coordination reduces the polarity of the metal ion and increases the lipophilicity of the complex. This allows preferential penetration through the more fluid, negatively charged membranes of cancer cells. Consequently, the complexes reach lethal intracellular concentrations in malignant cells more effectively than in normal cells, explaining the observed selectivity.

Co(II)-AHMT and **Cu(II)-AHMT** complexes exhibit reduced cytotoxicity, underscoring the metal-dependent nature of their antitumor effects. The **Ni(II)-AHMT** complex exhibits potency comparable to that of doxorubicin (DOX) in MCF-7 cells (8.70 *vs.* 4.17 μM), indicating its potential as a targeted chemotherapeutic agent. The selectivity index of **Ni(II)-AHMT** toward MCF-7 cells, is approximately 14.3, indicating that the compound is about fourteen times more toxic to cancer cells than to normal cells and therefore exhibits high selectivity and a potentially

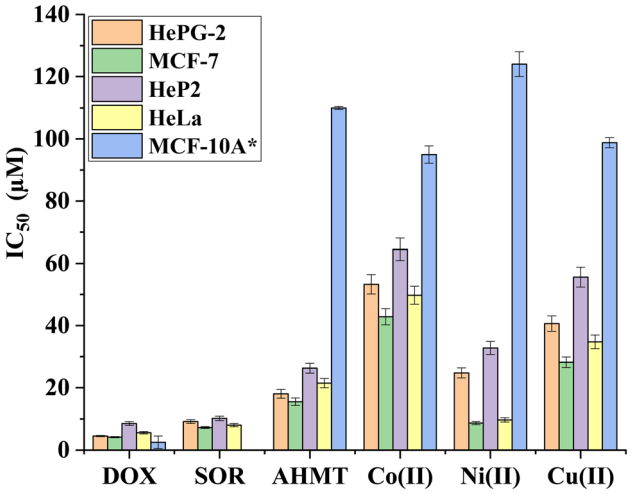

Fig. 11 Cytotoxicity IC_{50} (μM) of AHMT and its metal complexes.

favorable safety margin, suggesting that **Ni(II)-AHMT** exerts its anticancer effects through ligand-specific mechanisms rather than nonspecific nickel toxicity, as free Ni^{2+} ions typically exhibit much lower selectivity and higher toxicity toward normal cells. These trends align with research indicating that triazole-metal complexes often enhance cytotoxicity by stabilizing ligand–metal interactions and selectively targeting cells.[52]

3.4.3. Apoptosis assay and cell cycle analysis. Cycle and apoptosis analyses (Fig. 12 and 13) have been conducted on the **Ni(II)-AHMT** complex to investigate the mechanism of cytotoxicity. Whereas, flow cytometry results show that the **Ni(II)-AHMT** complex induces cytotoxicity in MCF-7 breast cancer cells by arresting the cell cycle specifically at the G1 phase. Whereas, Ni(II) complex triggered a substantial accumulation of cells in the G0–G1 phase (81.96%) compared to the untreated control (59.38%). Consequently, there was a significant lessening in the percentage of cells progressing to the S phase (13.39% *vs.* 28.75% in the control) and to the G2/M phase (4.65% *vs.* 11.87% in the control). On the other hand, the cell death mechanism induced by **Ni(II)-AHMT** is primarily apoptosis rather than necrosis, a desirable characteristic for potential pharmacophores. The obtained data show that **Ni(II)-AHMT** induced a total apoptosis rate of 31.61%, representing a substantial increase over the 2.77% observed in spontaneous apoptosis in control cells.

3.4.4. Superoxide (SOD)-like activity. The **AHMT** ligand and its metal complexes exhibit substantial superoxide dismutase (SOD) activity (Fig. 14 and Table S4), with efficacy varying depending on metal coordination. The unbound ligand exhibits significant radical-scavenging ability, attaining 75.8% inhibition, which is equivalent to the reference antioxidant L-ascorbic acid at 78.2%. Nickel coordination (**Ni(II)-AHMT**) maintains high activity (70.2%), but **Cu(II)-AHMT** (42.9%) and **Co(II)-AHMT** (30.9%) complexes exhibit diminished efficacy.

This metal-dependent trend corresponds to SOD processes, in which nickel's redox versatility facilitates effective superoxide disproportionation *via* cyclic Ni(II)/Ni(III) transitions, whereas cobalt's diminished activity may arise from reduced metal–ligand cooperativity in electron transfer. The ligand's independent efficacy indicates that its mercapto and hydrazino groups facilitate radical stabilization, possibly *via* hydrogen bonding or direct electron donation. These findings underscore **AHMT**'s dual function as an active antioxidant and a framework for modulating metal-specific SOD activity, with nickel complexes demonstrating notable potential for alleviating oxidative stress.[54,55]

3.4.5. Antioxidant activity. The DPPH assay results demonstrate the antioxidant activity of the **AHMT** ligand and its metal complexes, assessed by their efficacy in scavenging free radicals at different doses (Fig. 15 and Table S5). The unbound ligand (**AHMT**) exhibits significant radical scavenging efficacy, achieving an inhibition rate of 98.1% at 100 μM and an IC_{50} value of 20.90 ± 0.14 μM, signifying a robust antioxidant capability comparable to that of the reference vitamin C (IC_{50} = 16.81 ± 0.10 μM). The **Ni(II)-AHMT** complex exhibits notable activity, achieving 92.8% inhibition at 100 μM and an IC_{50} of 27.81 ± 0.19 μM, surpassing both **Cu(II)-AHMT** (IC_{50} = 33.51 ± 0.22 μM) and **Co(II)-AHMT** (IC_{50} = 62.05 ± 0.48 μM), which demonstrate increasingly diminished antioxidant properties. The data indicate that nickel coordination marginally reduces but predominantly maintains the ligand's antioxidant activity,

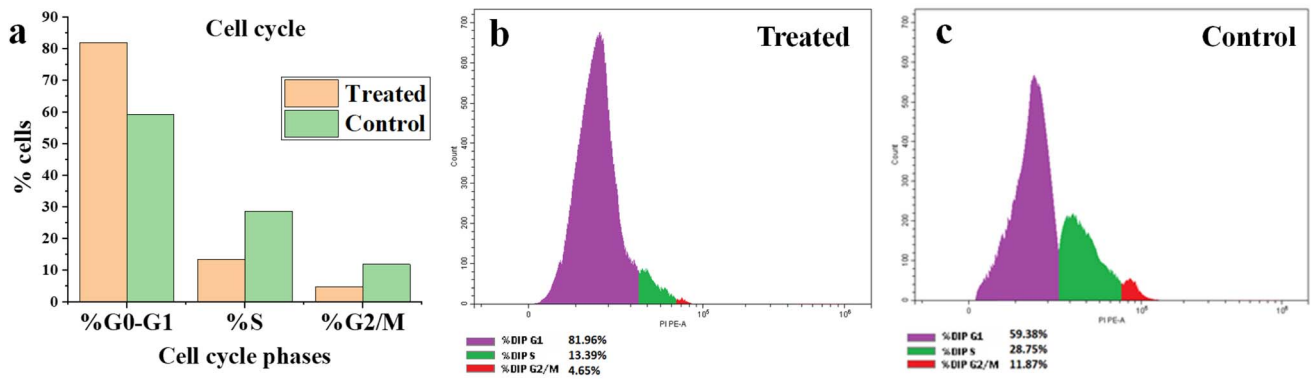

Fig. 12 Cell cycle phases diagrams, (a) plot of cell cycle phases percentages of treated and untreated cells, (b) treated cells with Ni-AHMT, (c) untreated MCF-7 cells.

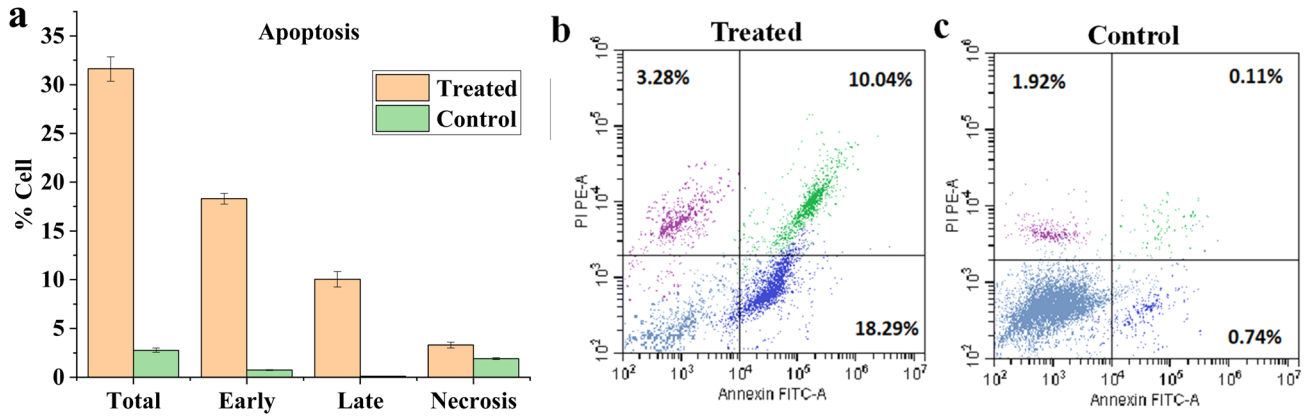

Fig. 13 Apoptosis dot plots of MCF-7 cells: (a) quantification of total, early, and late apoptosis, as well as necrosis, in treated and untreated cells, (b) cells treated with **Ni-AHMT**, (c) untreated cells.

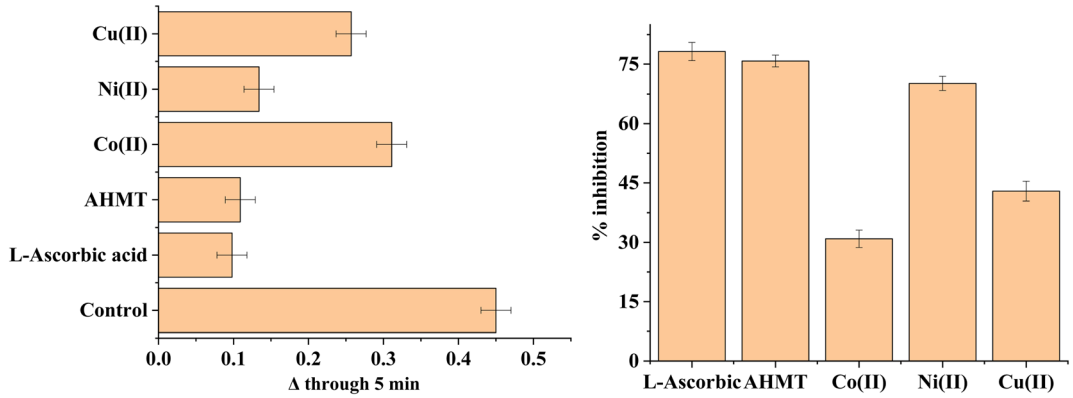

Fig. 14 Superoxide (SOD)-like activity of **AHMT** and its isolated complexes.

whereas cobalt complexation substantially diminishes it. The DPPH assay substantiates the robust free radical scavenging capacity of the **AHMT** ligand and underscores the role of metal ions in altering its antioxidant characteristics.

3.4.6. Colorimetric assay for DNA binding affinity. The DNA affinity of the **AHMT** ligand and its metal complexes was assessed using a DNA/methyl green displacement assay, with IC_{50} values denoting the concentration necessary to displace 50% of the dye (Fig. 16 and Table S6). The findings indicate that the **Ni(II)-AHMT** complex demonstrates the most potent DNA binding among the evaluated drugs, with an IC_{50} of 38.32 ± 1.7 μM, closely rivaling the reference medication doxorubicin (DOX), which has an IC_{50} of 31.54 ± 1.5 μM. The unbound ligand **AHMT** exhibits a moderate binding affinity of 41.85 ± 1.9

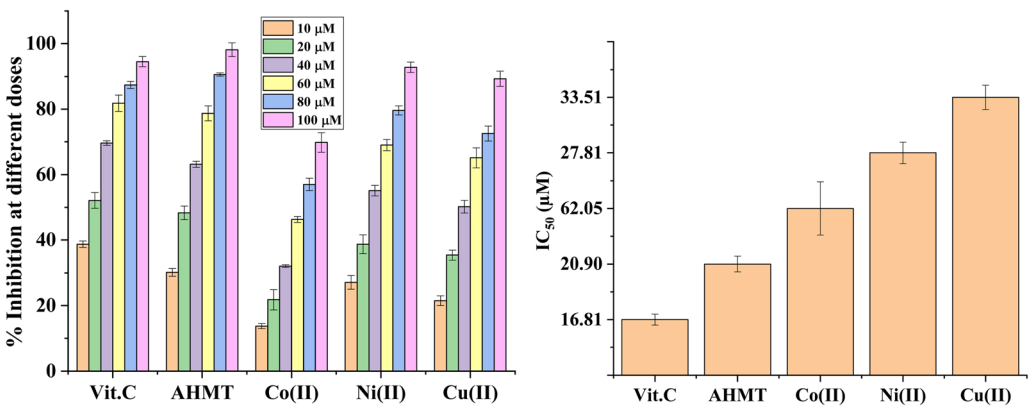

Fig. 15 Antioxidant activity of **AHMT** and its isolated complexes.

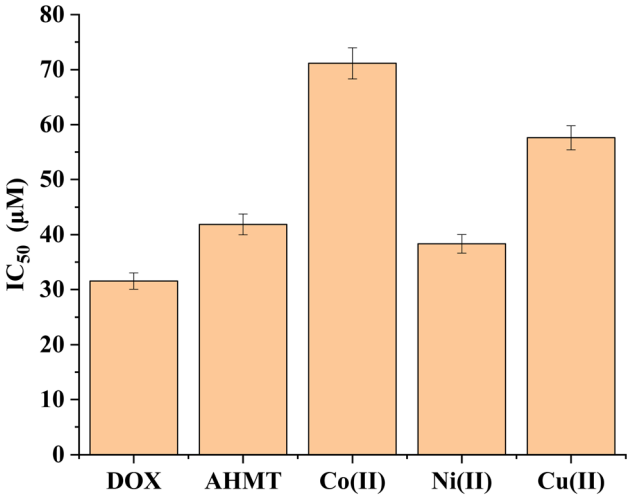

Fig. 16 DNA/methyl green colorimetric assay of AHMT and isolated complexes.

μM, but the **Cu(II)-AHMT** and **Co(II)-AHMT** complexes display increasingly diminished interactions with DNA, with IC_{50} values of 57.60 ± 2.2 μM and 71.13 ± 2.8 μM, respectively. This pattern indicates that nickel coordination amplifies the ligand's capacity to bind with DNA, possibly *via* enhanced intercalation or groove binding, whereas copper and cobalt complexes diminish this affinity. These findings underscore the importance of metal ion selection in shaping the DNA-binding properties of triazole-based drugs, with nickel complexes demonstrating significant potential for DNA-targeted therapeutic applications.

3.5. Molecular docking studies

3.5.1. DNA binding. Cytotoxic agents are thought to exert their effects by binding to DNA base pairs. Intercalation and groove binding are two main binding modes of metal complexes, including Co(II), Ni(II), and Cu(II), with DNA. Metal complexes can interact with DNA *via* covalent hydrogen bonds (HB) or non-covalent electrostatic forces.[30] Intercalator metal complexes can effectively insert into the base pairs of the DNA double helix, disrupting its function.[56] Groove binders disrupt DNA replication and transcription and, accordingly, can induce apoptosis and cell cycle arrest, making them effective cytotoxic and antimicrobial agents.[57,58] Metal complexes could also bind within the grooves of the DNA double helix. The positively charged metal and the negatively charged phosphate backbone may also interact *via* electrostatic forces. The presence of an aromatic ligand, such as 1,2,4-triazole, bound to a metal is expected to enhance DNA binding affinity through intercalation.[59,60] Considering these proven scientific facts, we decided to evaluate the potential DNA-binding activity of 4-amino-3-hydrazino-5-mercapto-1,2,4-triazole (**AHMT**) and its complexes with Co(II), Ni(II), and Cu(II). This has been conducted *in vitro*, and the obtained results were validated and rationalized using *in silico* methods, including molecular docking. The free ligand (**AHMT**) acted as a DNA groove binder through the formation of three hydrogen bonding interactions within a distance range of 2.89–3.28 Å. The terminal primary amine functionality of the hydrazine group (NH–NH_2) formed one HB with the nucleotide base DA10, whereas the adjacent secondary NH group of the hydrazine side chain built another HB with the amidic C=O group of thymine (DT31). In the last HB interaction, the NH_2 group attached to *N*-4 of **AHMT** served as a hydrogen bond donor, while the carbonyl group of cytosine (DC32) served as an acceptor. The docking score for this ligand was −4.21 kcal mol^{-1}. The cobalt complex **Co(II)-AHMT** displayed −3.90 kcal mol^{-1} as a free energy of binding and interacted with DNA through a set of four HB interactions. This metal complex interacted with the DNA nucleotide bases DG37, DA5, and DG6. In this set of HBs, the terminal hydrazine moieties of **Co(II)-AHMT** acted as HB donors in two interactions, whereas in the other two, one of its chlorine atoms served as an acceptor. Fig. 17 displays the extraordinary mixed approach of intercalation and groove-binding pattern of the 1,2,4-triazole-nickel complex **Ni(II)-AHMT**. This ligand displayed the highest docking score (−4.42 kcal mol^{-1}) and interacted with DNA by five HBs and one π-H stacking contact. A bidirectional HB has been observed between the nucleotide base DG4 and both chlorine atoms of the metal complex. One of the terminal hydrazine moieties formed a HB with the nucleotide base guanine DG6, while the mercapto group acted as a HB acceptor to build one more HB with DG38 within 4.22 Å. A π-H stacking contact has been formed between this nickel complex and adenine nucleotide base (DG3). The relatively high docking score and the extraordinary interaction pattern of this **Ni(II)-AHMT** complex may help rationalize the better *in vitro* results of this ligand in DND binding and cytotoxicity assessments.

The copper complex **Cu(II)-AHMT** displayed a relatively lower binding energy (−2.24 kcal mol^{-1}) and revealed five HBs and one π-H stacking interaction. The HB donor groups of this ligand interacted with the nucleotide bases DA10, DT12, DC13, DC32, and DT31, whereas the π-H stacking has been developed between the 1,2,4-triazole core and the pyrimidine ring of DT31. Table S7 summarizes the docking scores, interaction distances, interacting nucleotides, and interaction types for the free ligand **AHMT** and its metal complexes.

3.5.2. β-Lactamases inhibition. One major mechanism of microbial resistance to commonly prescribed antibiotics is the production of β-lactamases, a group of enzymes that hydrolyze β-lactam antibiotics, rendering them ineffective.[61] A wide range of bacteria, such as *E. coli* and *S. aureus*, can develop this type of antibiotic resistance. Thus, we decided to investigate the virtual binding of **AHMT** and its metal complexes, **Co(II)-AHMT**, **Ni(II)-AHMT**, and **Cu(II)-AHMT**, with β-lactamases. **AHMT** exhibited a docking score of −4.00 kcal mol^{-1} and displayed two HBs and two π-H stacking interactions with the biological target studied. *N*-1 and the terminal amino group of the hydrazine functionality in **AHMT** worked as HB acceptors to form two interactions with the amino acid residues Gly236 and Arg244. Within 3.47 Å, one hydrophobic interaction developed between the aromatic ring of Tyr105 and the *N*-4 attached amine in **AHMT**. One additional hydrophobic interaction formed between the 1,2,4-triazole ring and the aliphatic side chain of Ala237. This virtual binding pattern may support the relatively wider-diameter *in*

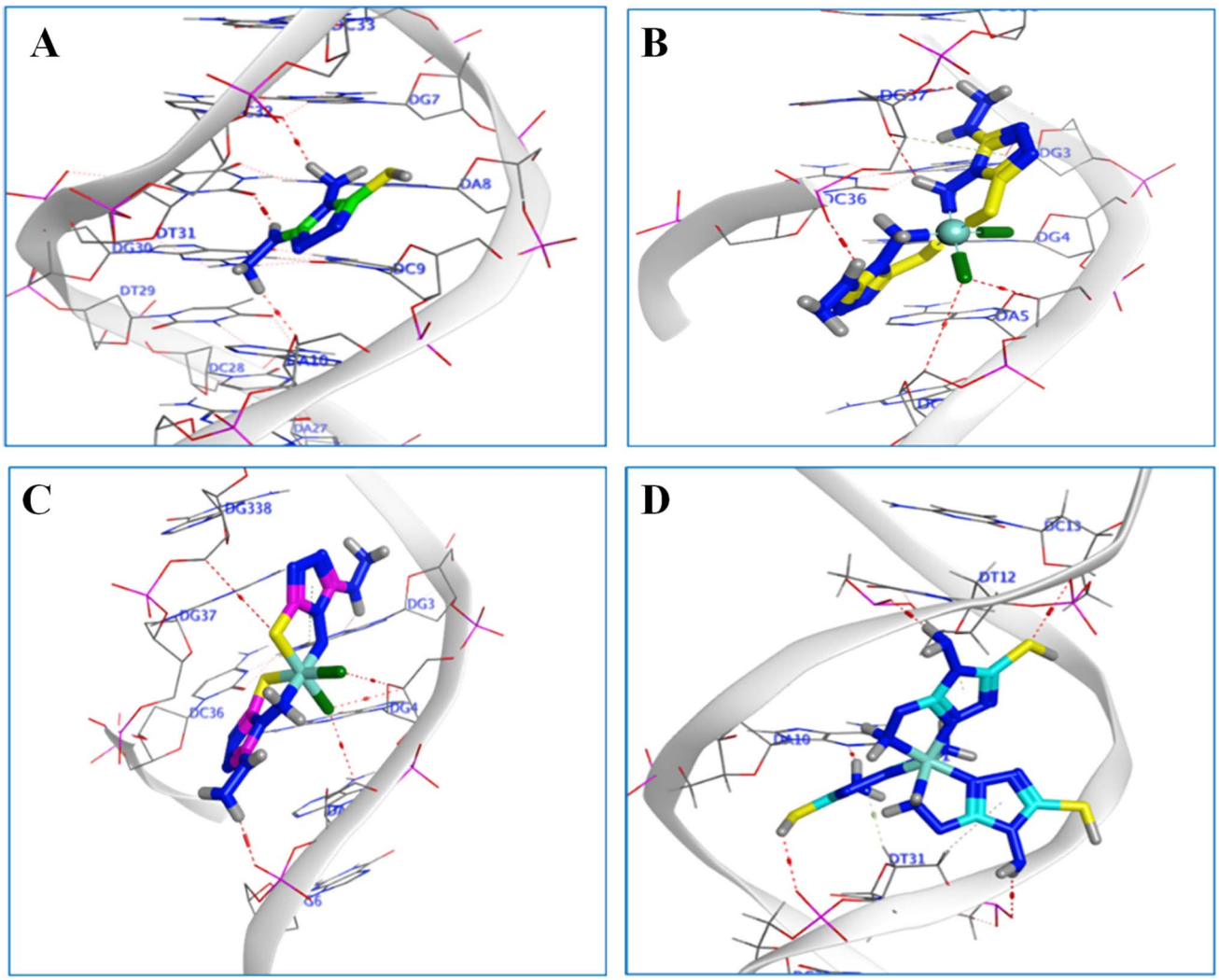

Fig. 17 3D interaction patterns of AHMT (A), Co(II)-AHMT (B), Ni(II)-AHMT (C), and Cu(II)-AHMT (D) with DNA double helix.

vitro inhibition zones of **AHMT** against *E. coli* (9.00 mm) and *S. aureus* (11 mm). **Co(II)-AHMT** produced the lowest docking score (−3.11 kcal mol^{-1}) and displayed five hydrogen bonds and one ionic (electrostatic) interaction with five amino acid residues of *E. coli* β-lactamase (Met272, Glu104, Glu240, Asn132, and Tyr105). This result is almost consistent with the *in vitro* antimicrobial testing. Conversely, the nickel complex **Ni(II)-AHMT** has shown the best combined results (scoring energy = −5.77 kcal mol^{-1}; RMSD = 1.88; Table S8). Six HBs and one hydrophobic interaction have been built between this antimicrobial candidate and the amino acid backbones of *E. coli* β-lactamase. One of the terminal hydrazine functionalities of **Ni(II)-AHMT** acted as HB donor/acceptor to form three covalent interactions with Asn170 and Glu166 residues within 2.81–3.10 Å. Ser130 and Ser235 residues developed two favorable HB interactions with **Ni(II)-AHMT** within 3.59 and 2.77 Å, respectively. The aliphatic chain of Ala239 formed one π-H stacking contact with the 1,2,4-triazole ring of **Ni(II)-AHMT**. This unique interaction profile contributes to rationalizing the superior *in vitro* activity of **Ni(II)-AHMT** in antimicrobial testing (% activity indices for *E. coli* and *S. aureus* = 46.1% and 58.30%, respectively). With −5.53 kcal mol^{-1} as a free energy of binding, **Cu(II)-AHMT** interacted with β-lactamase through a set of covalent and non-covalent interactions. Glu104 served as an HB donor and an anionic partner, forming three hydrogen bonds and five ionic interactions. Likewise, Glu240 formed an additional hydrogen bond and one more ionic interaction, whereas Asn170 and Asn132 acted as HB donors and acceptors, forming two covalent bonds. Table S8 and Fig. 18 show the detailed docking results of **AHMT**, **Co(II)-AHMT**, **Ni(II)-AHMT**, and **Cu(II)-AHMT** into *E. coli* β-lactamase.

3.5.3. Binding with human serum albumin (HSA). Because of its ability to bind and transport anticancer, antimicrobial, and other medications, human serum albumin (HSA) is considered a key determinant and a major contributor to drug delivery and pharmacokinetics.[62] Considering this importance, we examined the *in silico* binding potential of **AHMT** and its metal complexes, **Co(II)-AHMT**, **Ni(II)-AHMT**, and **Cu(II)-AHMT**, to HSA and compared them with the native HSA binder, warfarin. Results of docking experiments showed that the

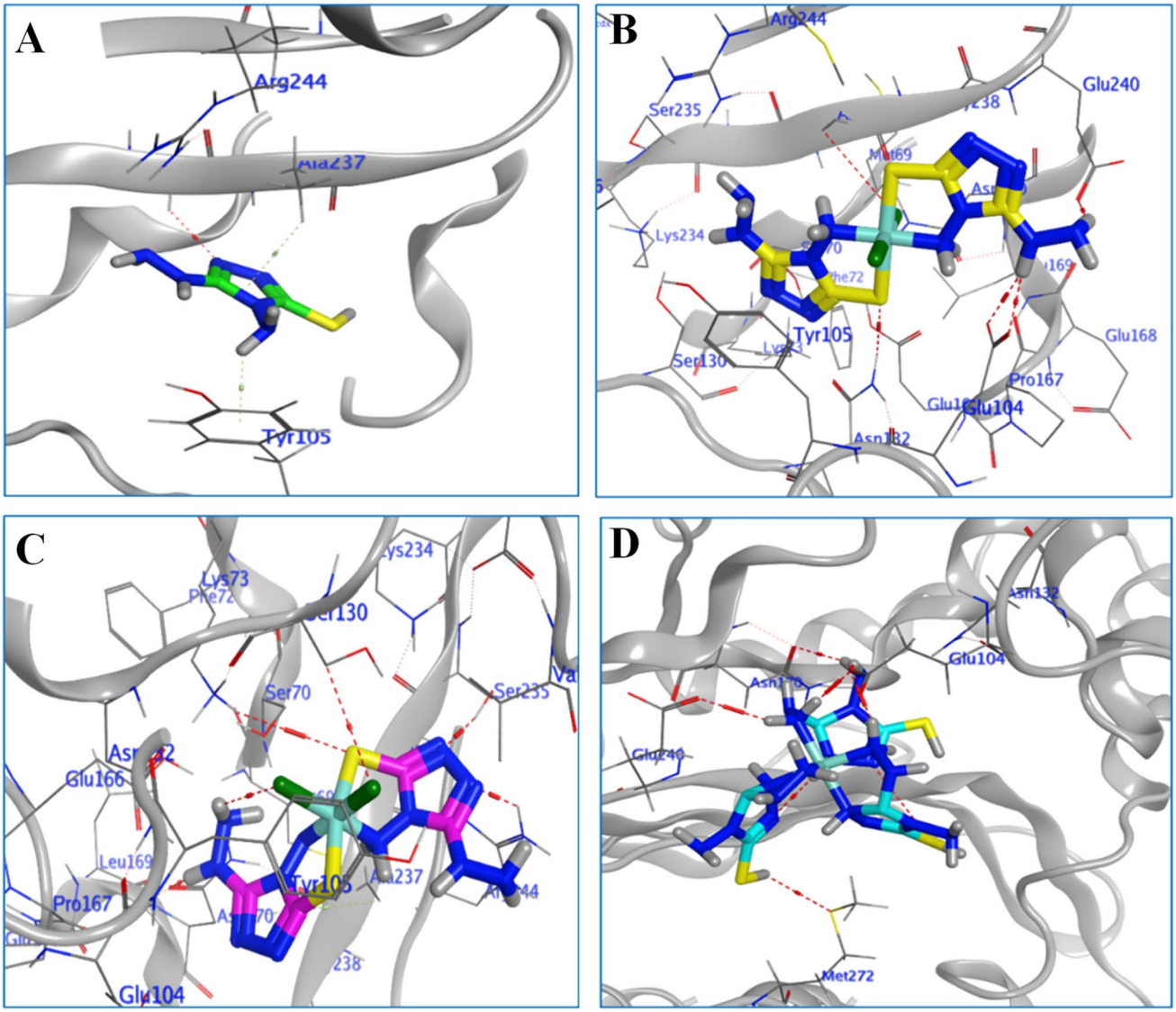

Fig. 18 3D interaction patterns of **AHMT** (A), **Co(II)-AHMT** (B), **Ni(II)-AHMT** (C), and **Cu(II)-AHMT** (D) with *E. coli* β-lactamase.

original warfarin–HSA complex (Fig. 19) shows three classical HBs with Tyr150, Arg222, and Lys199 and one hydrophobic interaction with Ala291.[62]

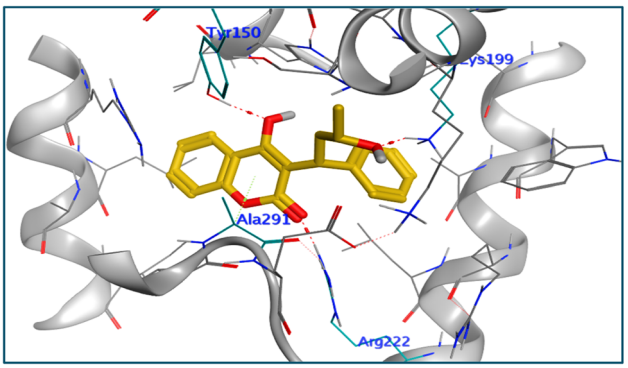

Fig. 19 Binding pattern of warfarin with the HSA. HBs are shown as red dotted lines, while hydrophobic interactions are shown as faint green dotted lines.

The binding interaction of **AHMT** with HSA (Fig. 20) includes a conventional HB with the amino acid Ser192 within 3.27 Å, and one hydrophobic interaction with Lys195 within 4.29 Å. The critical amino acid residues included in the binding interaction of warfarin (Ala291, Lys199, and Arg222) were also found in the binding interactions of **Co(II)-AHMT** and **Cu(II)-AHMT** with HSA. The triazole ring in each ligand interacted through hydrophobic stacking with the aliphatic chain of Ala291. **Ni(II)-AHMT** displayed one of the highest docking scores (−4.06 kcal mol^{-1}; Table S9), indicating its potential to effectively bind with HSA, and consequently better distribution and delivery. Fig. 20 shows the detailed docking results of **AHMT**, **Co(II)-AHMT**, **Ni(II)-AHMT**, and **Cu(II)-AHMT** into the active pocket of HSA.

3.6. Structure–activity relationships (SAR)

The biological activities of **AHMT** and its Co(II), Ni(II), and Cu(II) complexes are intricately associated with their structural characteristics, which affect stability, solubility, and interactions

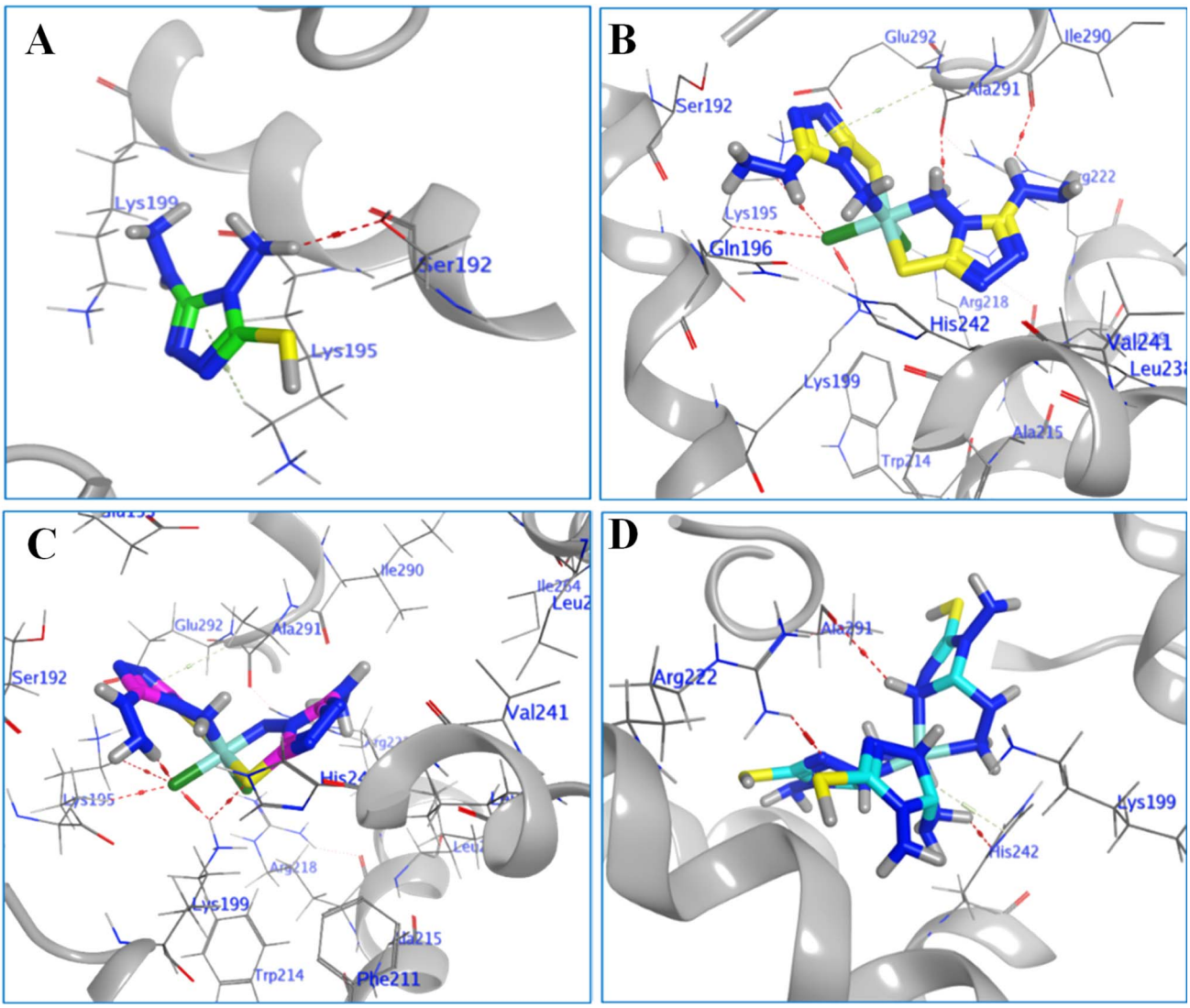

Fig. 20 3D interaction patterns of AHMT (A), Co(II)-AHMT (B), Ni(II)-AHMT (C), and Cu(II)-AHMT (D) into the active pocket of HSA.

with targets. The planar triazole core of **AHMT** facilitates π–π stacking and hydrogen bonding with biomolecular targets such as DNA. Additionally, its amino (–NH_2), hydrazino (–NH–NH_2), and mercapto (–SH) groups offer various coordination sites for metal binding and radical scavenging. [Ni(**AHMT**)$_2$Cl$_2$]·H_2O (**Ni(II)-AHMT**) and [Co(**AHMT**)$_2$Cl$_2$] (**Co(II)-AHMT**) exhibit a monomeric octahedral structure, incorporating two bidentate **AHMT** ligands alongside two chloride ions. This configuration enhances DNA groove binding and β-lactamase inhibition by optimizing the balance of hydrophobicity and charge distribution. On the other hand, [Cu(**AHMT**)$_3$]Cl$_2$ (**Cu(II)-AHMT**) displays a cationic octahedral geometry coordinated by three **AHMT** ligands. The charged nature of DNA enhances electrostatic interactions; however, steric hindrance from the three ligands may diminish binding efficiency to enzymatic targets such as SOD. Moreover, the d^8 configuration of Ni(II) enhances ligand field stabilization and promotes redox inactivity, thereby supporting the formation of stable DNA adducts and prolonged antimicrobial effects. In contrast, the d^9 configuration of Cu(II) facilitates redox cycling, contributing to oxidative stress-mediated cytotoxicity but with lower selectivity. The hydrazino group in **AHMT** enhances the stability of metal chelation, whereas the mercapto group contributes to antioxidant activity through radical-scavenging mechanisms. The combination of these groups in **Ni(II)-AHMT** yields 70–75% SOD-like inhibition, surpassing that of Co(II) and Cu(II) analogs. Consequently, the structural insights elucidate **Ni(II)-AHMT**'s enhanced DNA-binding efficacy through groove interactions, its antimicrobial activity *via* β-lactamase inhibition, and its cytotoxicity, with an IC_{50} of approximately 8–9 μM against MCF-7/HeLa cells. The findings highlight the importance of metal–ligand coordination geometry and electronic properties in optimizing triazole-based therapeutics. The selectivity of the synthesized **AHMT** complexes toward malignant cell lines over normal cells can be rationalized through the synergy between Tweedy's chelation theory[50] and cancer cell physiology. The increased lipophilicity of the chelates facilitates uptake across the hyperpolarized, fluid membranes of cancer cells. Furthermore, the acidic

microenvironment characteristic of tumor tissues likely promotes the selective intracellular release of the metal ions. Once internalized, these complexes induce targeted apoptosis by exploiting the high basal oxidative stress levels of cancer cells, a mechanism that normal cells are better equipped to resist due to their robust homeostatic and antioxidant capacities.

4. Conclusion

In conclusion, the synthesis and evaluation of 4-amino-3-hydrazino-5-mercapto-1,2,4-triazole (**AHMT**) and its Co(II), Ni(II), and Cu(II) complexes demonstrate their significant potential in biomedical applications. Structural characterization confirmed the proposed configurations of the compounds, while biological assays highlighted **Ni(II)-AHMT** as the most promising candidate. It exhibited superior antibacterial and fungal activity, and strong DNA-binding affinity, suggesting that DNA is a key biotarget. Notably, both **AHMT** and **Ni(II)-AHMT** displayed remarkable antioxidant activity *via* superoxide dismutase (SOD) mimicry, achieving ~75% inhibition in radical-scavenging assays. Interestingly, **Ni(II)-AHMT** exhibited potent cytotoxicity against MCF-7 and HeLa cancer cell lines (IC_{50} values of 8.70 ± 0.5 μM and 9.72 ± 0.7 μM, respectively), as evidenced by a pronounced G0/G1 cell-cycle arrest (81.96% *vs.* 59.38% in control) accompanied by a strong induction of apoptosis (total apoptotic cells 49.90% *vs.* 3.51% in control), highlighting its potential as a promising apoptotic and cell-cycle-modulating agent. Molecular docking studies further validated these findings, revealing **Ni(II)-AHMT**'s potential as a DNA groove binder and antimicrobial agent through stable interactions with biological targets like β-lactamase and human serum albumin. These results position **Ni(II)-AHMT** as a multi-faceted therapeutic candidate, combining antimicrobial, anti-cancer, and antioxidant properties. Future *in vivo* studies are warranted to explore its pharmacokinetics, safety profile, and efficacy in complex biological systems, paving the way for novel drug development inspired by 1,2,4-triazole-based metal complexes.

Ethical approval

We have no financial conflicts or personal connections to declare. Also, this research did not involve the use of either humans/or animals. The biological assays were conducted in strict accordance with the guidelines and approval of the Ethics Committee at Mansoura University (Faculty of Science). No material was extracted from live vertebrate animals.

Conflicts of interest

The authors declare that they have no known competing financial interests or personal relationships that could have influenced the work reported in this paper.

Data availability

The data are in the supplementary information (SI). Supplementary information: spectroscopic data of the compounds, materials, and methods. See DOI: https://doi.org/10.1039/d5ra09383j.

Acknowledgements

This research was supported by Royal Society of Chemistry Research Fund grants through project (R23-0040908760) (Azza A. Hassoon) and project (R25-3563728902) (Azza A. Hassoon).

References

1 L. Todorov and I. Kostova, *Front. Chem.*, 2023, **11**, 1247805.
2 A. Kumar, S. Devi, S. Kumar and K. Lal, *Coord. Chem. Rev.*, 2025, **536**, 216675.
3 S. M. El Rayes, *Molecules*, 2010, **15**, 6759–6772.
4 H. Benaissa, N. N. Adarsh, K. Robeyns, J. J. Zakrzewski, S. Chorazy, J. G. M. Hooper, F. Sagan, M. P. Mitoraj, M. Wolff, S. Radi and Y. Garcia, *Cryst. Growth Des.*, 2021, **21**, 3562–3581.
5 C. Amaral, C. F. Almeida, M. J. Valente, C. L. Varela, S. C. Costa, F. M. Roleira and G. Correia-da-Silva, *Cancers*, 2025, **17**, 165.
6 T. Hosseinnejad, F. Ebrahimpour-Malmir and B. Fattahi, *RSC Adv.*, 2018, **8**, 12232–12259.
7 E. A. Ghaith, A. B. Abdallah, A. A. El-Sawi and G. G. El-Bana, *J. Heterocycl. Chem.*, 2025, **62**, 1863–1875.
8 L. Qi, M.-C. Li, J.-C. Bai, Y.-H. Ren and H.-X. Ma, *Bioorg. Med. Chem. Lett.*, 2021, **40**, 127902.
9 D. Domyati, S. A. Zabin, A. A. Elhenawy and M. Abdelbaset, *Processes*, 2021, **9**(6), 1008.
10 R. R. Radwan, N. H. Zaher and M. G. El-Gazzar, *Chem.-Biol. Interact.*, 2017, **274**, 68–79.
11 M. Ajmal, U. Yunus, R. M. Graham and R. M. Leblanc, *ACS Omega*, 2019, **4**(27), 22280–22291.
12 P. C. Jilloju, L. Persoons, S. K. Kurapati, D. Schols, S. D. Jonghe, D. Daelemans and R. R. Vedula, *Mol. Diversity*, 2022, **26**, 1357–1371.
13 A. Mermer and S. Demirci, *Eur. J. Med. Chem.*, 2023, **259**, 115655.
14 Y. Feng, L. Wu, Y. Luo, Y. Hao, P. Zhang, R. Zeng and S. Chen, *Talanta*, 2025, **291**, 127858.
15 C. Liu, J. Huang, J. Chen, Q. Xue, H. Yan, D. Kong, Z. Ma, W. Shen, H. K. Lee and S. Tang, *ACS Sens.*, 2025, **10**(3), 2060–2072.
16 M. Z. Abedeen, M. Sharma, H. S. Kushwaha and R. Gupta, *TrAC, Trends Anal. Chem.*, 2024, **176**, 117729.
17 P. Srinivasan, S. P. Sivaraman, D. K. Madhu, P. Sengupta, B. Kattela, S. Nagarajan, A. M. Mohan and P. Deivasigamani, *J. Hazard. Mater.*, 2024, **469**, 133960.
18 P. Kumar and H. K. Sharma, *Electrochim. Acta*, 2013, **87**, 925–929.
19 Vinita, M. Tiwari and R. Prakash, *Appl. Surf. Sci.*, 2018, **449**, 174–180.

20 G. B. Bagihalli, P. S. Badami and S. A. Patil, *J. Enzyme Inhib. Med. Chem.*, 2009, **24**, 381–394.
21 L. Calu, M. Badea, M. C. Chifiriuc, C. Bleotu, G.-I. David, G. Ionita, L. Marutescu, V. Lazar, N. Stanica, I. Soponaru, D. Marinescu and R. Olar, *J. Therm. Anal. Calorim.*, 2015, **120**, 375–386.
22 J.-K. Wang, C.-H. Wang, C.-C. Wu, K.-H. Chang, C.-H. Wang, Y.-H. Liu, C.-T. Chen and P.-T. Chou, *J. Am. Chem. Soc.*, 2024, **146**, 3125–3135.
23 H. S. Biswal and S. Wategaonkar, *J. Phys. Chem. A*, 2009, **113**, 12763–12773.
24 K. Mazmanian, K. Sargsyan, C. Grauffel, T. Dudev and C. Lim, *J. Phys. Chem. B*, 2016, **120**, 10288–10296.
25 Y. Y. Zheng, Y. Wu, T. J. Begley and J. Sheng, *RSC Chem. Biol.*, 2021, **2**, 990–1003.
26 R. N. Pandey, R. N. Sharma, A. N. Sahey, S. Kumar, S. Kumar and S. Singh, *Asian J. Chem.*, 1993, **5**, 813–817.
27 A. B. J. Tadros, *J. Chem. Technol. Biotechnol.*, 1989, **45**, 213–221.
28 (*a*) L. Mishra and A. Kyadaw, *Proc. – Indian Acad. Sci., Chem. Sci.*, 2000, **112**, 449–458; (*b*) S. Sener, I. Kul and K. Bhat, *Synth. React. Inorg., Met.-Org., Nano-Met. Chem.*, 2015, **45**, 495–501.
29 B. H. Garg and P. K. Sing, *Synth. React. Inorg. Met.-Org. Chem.*, 1987, **17**, 923–936.
30 R. C. Varma and K. Varma, *Indian Chem. Soc., J.*, 1992, **69**, 577–578.
31 R. G. Dickinson and N. W. Jacobsen, *Org. Prep. Proced. Int.*, 1974, **6**, 156–157.
32 W. J. Geary, The use of conductivity measurements in organic solvents for the characterisation of coordination compounds, *Coord. Chem. Rev.*, 1971, **7**, 81–122.
33 R. V. Gadag and M. R. Gajendragad, *Curr. Sci.*, 1979, **2**, 839.
34 R. V. Gadag and M. R. Gajendragad, *Indian J. Chem., Sect. A*, 1980, **19A**, 705–707.
35 G. R. Burns, *Inorg. Chem.*, 1968, **7**, 277.
36 A. A. Hassoon, R. G. Harrison, N. Nawar, S. J. Smith and M. M. Mostafa, *J. Mol. Struct.*, 2020, **1203**, 127240.
37 A. A. Hassoon, S. J. Smith and R. G. Harrison, *Inorg. Chem. Commun.*, 2025, **178**, 114464.
38 A. A. Hassoon, S. J. Smith and R. G. Harrison, *RSC Adv.*, 2024, **14**, 31850–31860.
39 N. S. Al-Radadi, E. M. Zayed, G. G. Mohamed and H. A. Abd El Salam, *J. Chem.*, 2020, **1**, 1–12.
40 Y. Deswal, S. Asija, D. Kumar, D. K. Jindal, G. Chandan, V. Panwar, S. Saroya and N. Kumar, *Res. Chem. Intermed.*, 2022, **48**, 703–729.
41 K. Nakamoto, in *Infrared and Raman Spectra of Inorganic and Coordination Compounds, Part B: Applications in Coordination, Organometallic, and Bioinorganic Chemistry*, John Wiley & Sons, Inc., Hoboken, NJ, 6th edn, 2009.
42 J. Selbin, *J. Chem. Educ.*, 1964, **41**, 86–92.
43 J. R. Ferraro, *Low Frequency Vibrations of Inorganic and Coordination Compounds*, Plenum Press, New York, 1966.
44 A. B. P. Lever, *Inorganic Electronic Spectroscopy*, Elsevier, Amsterdam, 1984.
45 F. A. Cotton, G. Wilkinson, C. A. Murillo and M. Bochmann, *Advanced Inorganic Chemistry*, Wiley, New York, 6th edn, 1999.
46 W. Ferenc, A. W. Dziewulska, J. Sarzynski and B. Paszkowska, *Eclética Quím.*, 2006, **31**, 53–60.
47 M. Strzelecka and P. Świątek, *Pharmaceuticals*, 2021, **14**, 224.
48 A. Adak, V. Castelletto, B. Mendes, G. Barrett, J. Seitsonen and I. W. Hamley, *ACS Appl. Bio Mater.*, 2024, **7**, 5553–5565.
49 A. Adak, S. Ghosh, V. Gupta and S. Ghosh, *Biomacromolecules*, 2019, **20**, 1889–1898.
50 B. Tweedy, *Phytopathology*, 1964, **55**, 910–914.
51 A. Adak, G. Das, V. Gupta, J. Khan, N. Mukherjee, P. Mondal, R. Roy, S. Barman, P. K. Gharai and S. Ghosh, *J. Med. Chem.*, 2022, **65**, 13866–13878.
52 Z. H. Chohan and M. Hanif, *J. Enzyme Inhib. Med. Chem.*, 2010, **25**, 737–749.
53 Y. Draoui, S. Radi, Y. Bahjou, A. Idir, A. El Mahdaoui, A. Zyad, H. N. Miras, M. Ferbinteanu, A. Rotaru and Y. Garcia, *RSC Adv.*, 2023, **13**, 36158–36167.
54 V. Pelmenschikov and P. E. M. Siegbahn, *J. Am. Chem. Soc.*, 2006, **128**(23), 7466–7475.
55 P. O'Neill, E. M. Fielden, D. Cocco, G. Rotilio and L. Calabrese, *Biochem. J.*, 1982, **205**, 181–187.
56 Y. Thakur, R. Agrawal, M. Tripathi, M. K. Siddiqi, E. Mohapatra, R. H. Khan and R. Pande, *J. Mol. Struct.*, 2019, **1197**, 691–706.
57 X. Cai, P. J. Gray and D. D. Von Hoff, *Cancer Treat. Rev.*, 2009, **35**, 437–450.
58 M. P. Barrett, C. G. Gemmell and C. J. Suckling, *Pharmacol. Ther.*, 2013, **139**, 12–23.
59 W. Zafar, S. H. Sumrra and Z. H. Chohan, *Eur. J. Med. Chem.*, 2021, **222**, 113602.
60 P. P. Utthra, N. Pravin and N. Raman, *J. Photochem. Photobiol., B*, 2016, **158**, 136–144.
61 K. Bush, *Curr. Opin. Microbiol.*, 2010, **13**, 558–564.
62 R. D. Zanetti, G. A. da Cunha, M. B. Moreira, R. L. Farias, R. F. F. de Souza, P. R. D. V. de Godoy, M. S. Brassesco, F. V. Rocha, M. A. Lima, A. E. Mauro and A. V. G. Netto, *Polyhedron*, 2023, **229**, 116185.